

Controlling Interfacial Structural Evolution in Aqueous Electrolyte via Anti-Electrolytic Zwitterionic Waterproofing

Zheng Bo,* Meiqi Zhou, Shiyuan Zhou, Yajing Song, Zhu Liu, Honggang Liao,* Huachao Yang, Jianhua Yan, Kefa Cen, Xiulin Fan, Qian Yu, Kostya (Ken) Ostrikov, and Ju Li

Aqueous electrolytes are considered as an alternative to flammable and toxic organic electrolytes, whose broad applications in electrochemical energy storage (EES) devices unfortunately suffer from low electrochemical stability due to the easy electrolysis of water. Here, by performing in situ transmission electron microscope electrochemical characterizations at atomic resolution during charging/discharging, an anti-electrolytic strategy is revealed in aqueous electrolytes via physical zwitterionic waterproofing. It is found that the zwitterionic molecules can be directionally adsorbed to the negative electrode's surface under the applied electric field, forming strings of zwitterionic molecules that extract water out from the electrode. More zwitterionic molecules further aggregate at the outer end of the strings through intermolecular electrostatic interactions, forming a waterproof layer that successfully expels water from the electrode's surface. Meanwhile, the self-aggregation of zwitterionic additives in the bulk liquid successfully minimizes the influence on ion transport. Being intrinsically distinct from the solid electrolyte interphase concept associated with certain electrochemical reactions in organic or super-concentrated electrolytes, the strategy is effective in improving the electrochemical stability while maintaining high ionic conductivity in various aqueous electrolytes even with a dilute concentration, shedding light on developing sustainable EES devices with high performance.

conductivity, non-flammability, and large temperature range is required for liquid electrolyte used for high-performance and sustainable EES technologies.^[2] Aqueous electrolytes, which are intrinsically non-flammable, highly conductive, environmentally friendly and low-cost, have always been considered as a potential alternative to flammable and toxic liquid organic electrolytes.^[3] Unfortunately, free water in aqueous electrolytes has quite high reactivity with charged electrodes, whose thermodynamic electrochemical stability window is only 1.23 V that is $\approx 30\%$ that of the organic electrolyte.^[4] Building a protective solid-electrolyte interphase (SEI) layer at the electrode–electrolyte interface has been demonstrated as an effective route to prevent the continuous electrolysis of electrolytes.^[2c,5] However, such strategy is difficult to be applied in aqueous electrolytes since the easy electrolysis of free water continuously defeats the formation of robust SEI layer.^[4b,6]

Adding high concentration or certain type of salts had been proposed to facilitate the formation and repair of SEI layer on the electrode surface in aqueous electrolytes by enhancing chemical reaction of ions, especially the decomposition of anions, to overwhelm water electrolysis reaction.^[7] However, issues including the consumption of electrolytes, poor environmental adaptability, and

1. Introduction

Electrolyte plays an essential role in tuning the overall performance of electrochemical energy storage (EES) devices.^[1] The synergetic combination of wide voltage window, high ionic

conductivity, non-flammability, and large temperature range is required for liquid electrolyte used for high-performance and sustainable EES technologies.^[2] Aqueous electrolytes, which are intrinsically non-flammable, highly conductive, environmentally friendly and low-cost, have always been considered as a potential alternative to flammable and toxic liquid organic electrolytes.^[3] Unfortunately, free water in aqueous electrolytes has quite high reactivity with charged electrodes, whose thermodynamic electrochemical stability window is only 1.23 V that is $\approx 30\%$ that of the organic electrolyte.^[4] Building a protective solid-electrolyte interphase (SEI) layer at the electrode–electrolyte interface has been demonstrated as an effective route to prevent the continuous electrolysis of electrolytes.^[2c,5] However, such strategy is difficult to be applied in aqueous electrolytes since the easy electrolysis of free water continuously defeats the formation of robust SEI layer.^[4b,6]

Z. Bo, M. Zhou, H. Yang, J. Yan, K. Cen
State Key Laboratory of Clean Energy Utilization
College of Energy Engineering
Zhejiang University
Hangzhou 310027, China
E-mail: bozh@zju.edu.cn

S. Zhou, H. Liao
State Key Laboratory of Physical Chemistry of Solid Surfaces
Collaborative Innovation Center of Chemistry for Energy Materials
Xiamen University
Xiamen 361005, China
E-mail: hgliao@xmu.edu.cn

Y. Song, X. Fan, Q. Yu
Center of Electron Microscopy and State Key Laboratory of Silicon Materials
School of Materials Science and Engineering
Zhejiang University
Hangzhou 310027, China

Z. Liu
ZJU-Hangzhou Global Scientific and Technological Innovation Center
Hangzhou 311200, China

K. K. Ostrikov
School of Chemistry and Physics & Centre for Materials Science
Queensland University of Technology
Brisbane, Queensland 4000, Australia

J. Li
Department of Nuclear Science and Engineering and Department
of Materials Science and Engineering
Massachusetts Institute of Technology
Cambridge, MA 02139, USA

 The ORCID identification number(s) for the author(s) of this article can be found under <https://doi.org/10.1002/adfm.202207140>.

DOI: 10.1002/adfm.202207140

badly controllable kinetics remain unsolved.^[6a,8] In addition, since the competition between different chemical reactions (water electrolysis and decomposition of ions) relies on kinetics and is highly sensitive to environmental factors such as temperature and concentration, phase change of electrolyte in the form of gassing, freezing, or salt precipitation may occur even at ambient temperature.^[9]

As an alternative strategy, nonionic additives (e.g., sucrose molecules and polyethylene glycol) are used to directly confine the free water structure to suppress water electrolysis and expand the electrochemical stability windows via strong electrostatic interactions between water molecules and hydrophilic functional groups.^[10] However, the amount of free water in the bulk liquid phase is indiscriminately decreased, resulting in serious ion pairing and low conductivity of only 0.8–3.376 mS cm⁻¹.^[10] Such a trade-off is detrimental to the rate performance and power density of EES devices.^[11]

Here, by performing in situ transmission electron microscope electrochemical characterizations at atomic resolution upon charging/discharging, we revealed a mechanism for breaking the trade-off between electrochemical window and ionic conductivity in aqueous electrolytes via antielectrolytic zwitterionic waterproofing at the electrode surface with negligible influence on ion transport in bulk liquid. The formation mechanism of the nanometers' thick waterproof layer was studied by visualizing the dynamic behaviors of zwitterionic molecules near the electrode surface during charging/discharging at atomic resolution. Meanwhile, the zwitterionic molecules self-assembled into circular clusters, displaying negligible influence on ion transport. Consequently, the electrochemical stability window of the aqueous electrolyte was significantly increased to ≈ 2.83 V accompanied with high ionic conductivity up to 26 mS cm⁻¹. Being intrinsically distinct from the SEI mechanism associated with certain electrochemical reactions in organic or super-concentrated electrolyte, our mechanism is applicable to various aqueous electrolytes (e.g., NaNO₃, LiNO₃, KNO₃ and Li₂SO₄) even with a dilute concentration, shedding light on developing sustainable EES devices with high performance.

2. Results and Discussion

The zwitterionic additive here refers to a family of materials possessing anionic and cationic groups with different wettability, characterized by high dipole moments but are still charge neutral. As a typical example, betaine (C₅H₁₁NO₂), has a negatively charged, hydrophilic carboxyl (–COO⁻) group on one end, and a positively charged but hydrophobic trimethyl ammonium (–N⁺[CH₃]₃) group on the other end of the same monomeric unit (Figure 1a).^[12] Considering the unique zwitterionic nature of betaine additive, we expect that, as the electrode is negatively polarized, the hydrophobic positively charged –N⁺[CH₃]₃ groups of betaine would move toward the electrode surface due to the strong counterion–electrode coulombic interactions, while the water molecules could be expelled from the electrode surface since they favor the hydrophilic negatively charged –COO⁻ groups. Moreover, driven by the intermolecular electrostatic interaction, more betaine aggregations would continuously

connect to the ones preferentially adsorbed on the electrode surface at another end with hydrophilic negatively charged –COO⁻ group. Based on our density functional theory (DFT) calculations (see Experimental Section), the binding energy of the betaine molecule to itself is larger than that of the betaine to water, and the binding energy of betaine/ions is lower than that of the water/ions, indicating that clustering of betaine molecules should occur (The detailed results of the binding energy calculation are listed in Table S1, Supporting Information). In this way, an anti-electrolytic waterproof layer would physically form at the surface of the negatively charged electrode to reduce the free water in the interfacial region and suppress water electrolysis, which would be beneficial to the expansion of voltage window. On the other hand, the self-aggregated structure would rarely affect the original electrolyte environment in the bulk liquid phase and thus impart sufficient free water as solvent to transport charged ions.

Such a hypothesis is primarily supported by our molecular dynamics (MD) simulation. A simulation cell containing 189 Na⁺ ions, 189 NO₃⁻ ions, 726 betaine, and 5,252 water molecules was built to formulate the 2 M NaNO₃–0.9Betaine/H₂O electrolyte (Experimental Section), which was sandwiched between two graphene sheets as the negative and positive electrodes. An electric field $E_z = 0.2$ V nm⁻¹ was imposed along the z-axis of the electrolyte solutions with a thickness of ≈ 7.5 nm to mimic the experimental electrochemical condition. As shown in Figure 1b, high density of betaine molecules gathered at the interface, resulting in an obvious water-avoiding region between the negative electrode and the electrolyte. Consequently, the number density of water molecules at the interface was estimated to be $\approx 78\%$ lower than that of the bulk liquid region (detailed calculation can be found in Experimental Section). Such effect was absent at the positive electrode. Further increase of the electric field led to the penetration of cations through the waterproof layer (Figure S1, Supporting Information), realizing electrostatic adsorption at both electrodes and energy storage. With such an antielectrolytic zwitterionic waterproof layer, the cathodic limit potential and the overall electrochemical stability window of electrolyte should be expanded. Meanwhile, the solvation shell of Na⁺ or NO₃⁻ ions was maintained, leaving free water to separate ion pairing as shown in the right magnified window of Figure 1b. Following such principle, other zwitterionic additives, such as sulfobetaine (3-(Dimethyloctylazaniumyl)propane-1-sulfonate, C₁₃H₂₉NO₃S), should also perform the same (The relative binding energy calculation are listed in Table S2, Supporting Information).

Being distinct from the previous SEI concept relying on the chemical reactions of electrolytes, the above strategy is based on the formation of an anti-electrolytic waterproof layer through a physical process. Realizing this concept and describing it in real at molecular resolution, we constructed a micro-supercapacitor system in a liquid cell in high-resolution transmission electron microscope (HRTEM) for real-time observation by using acetylene black electrode and NaNO₃–Sulfobetaine/H₂O electrolyte, as schematically shown in Figure 1c. To enhance the mass-thickness contrast of TEM images and facilitate observations,^[13] sulfobetaine with heavier element (S) is used for in situ observations instead of betaine containing only light elements (C, H, O, and N). Similar to betaine, sulfobetaine also has a negatively

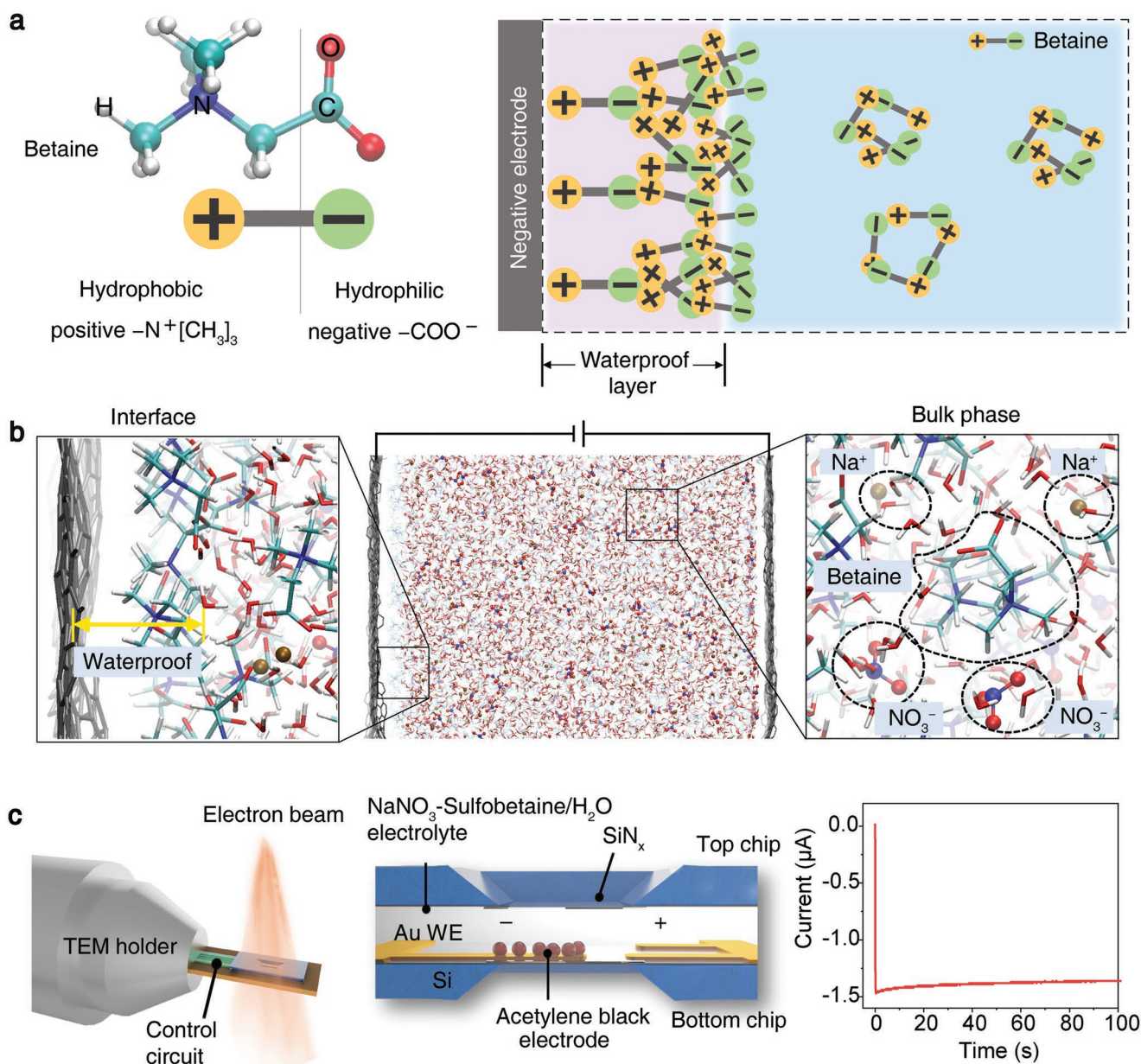


Figure 1. Overview of the zwitterionic additive strategy: schematic, MD simulation and the setup of in situ observations. a) Schematic of the zwitterionic additive strategy. b) Snapshots showing the structural picture of the 2 M NaNO_3 -0.9Betaine/ H_2O electrolyte under external electric field during MD simulations. The left and right windows display the magnified electrolyte structure at the solid-liquid interface and in the bulk liquid phase, respectively. c) Schematic of the in situ electrochemistry HRTEM holder and the liquid cell. The electrochemical cell was potentiostatic charged and discharged.

charged hydrophilic group and a positively charged but hydrophobic group on the same monomeric unit, which meets our concept of design. More details of the methods are presented in Experimental Section. In Figure S2 (Supporting Information), we present a series of HRTEM images showing the change of morphology of the electrode with atomic resolution during the negative polarization process. The corresponding in situ HRTEM movie was provided as Movie S1 (Supporting Information). Significant shrinkage of the electrode material was observed under electric field. Meanwhile, the surface of

the electrode material became rough with a gel-like structure attached to the crystallized acetylene black electrode. **Figure 2a** demonstrated the atomistic pictures of this evolution in details by showing the dynamic behaviors of sulfobetaine molecules upon charging. As a negative potential was applied on the electrode, we observed that considerable sulfobetaine molecules were attached to the surface of the loose acetylene black electrode, as marked by the white arrows in **Figure 2a**. It is noted that the length of one sulfobetaine molecule is ≈ 1 nm, therefore the black linear contrast here should refer to a string of several

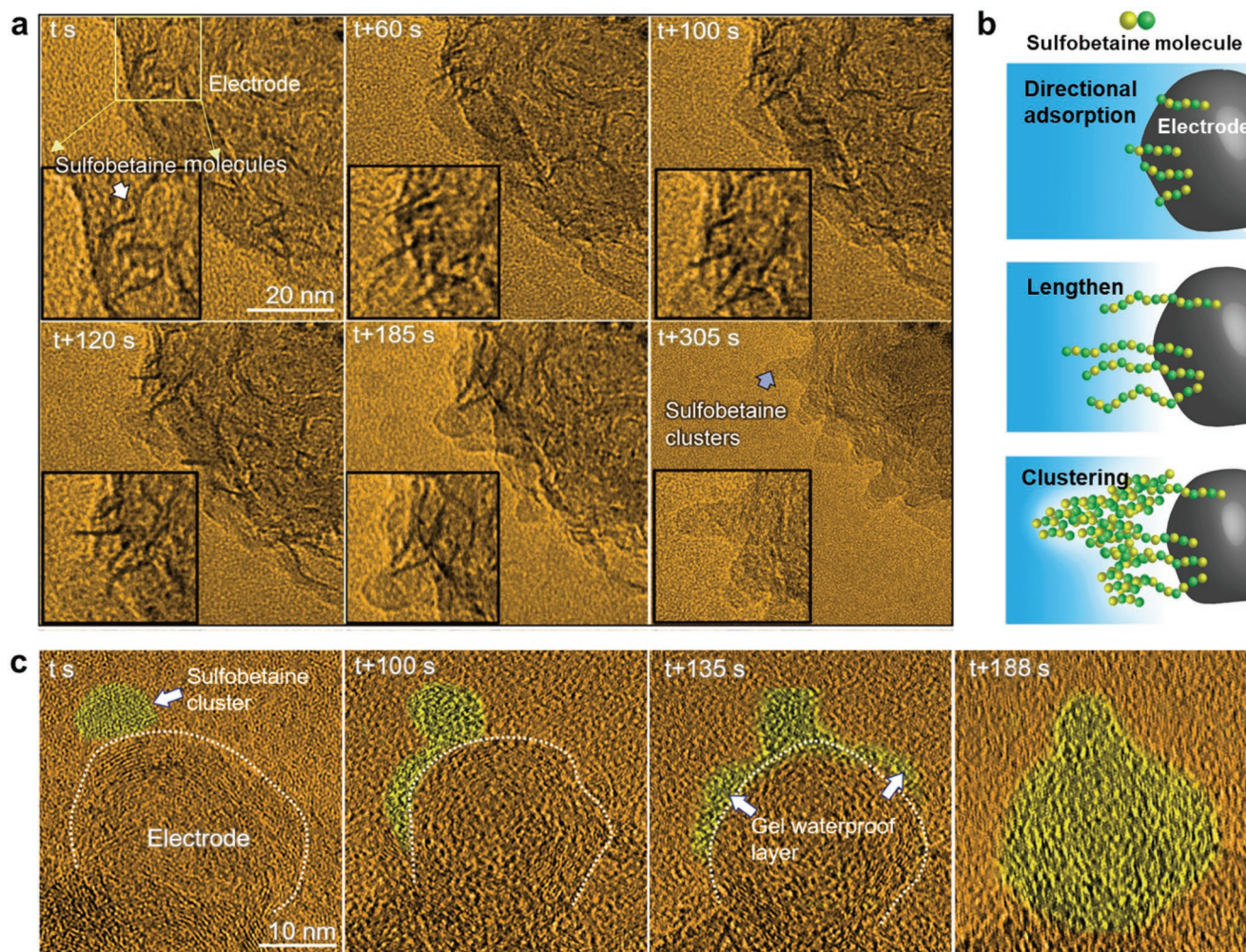


Figure 2. In situ atomic resolution HRTEM observation on the behaviors of sulfobetaine molecules at the solid-liquid interface under external electric field and the formation of the waterproof layer around the negative electrode surface. a) The dynamic behaviors of sulfobetaine molecules and the formation of the gel clusters were observed. The time-series atomic resolution images show the change of morphology of the electrode and the NaNO_3 -Sulfobetaine/ H_2O electrolyte during the negative polarization process. b) Schematic of the formation of sulfobetaine waterproof layer through three major stages: attach, lengthen and clustering. c) A series of in situ HRTEM images showing the structural change of a single acetylene black particle with atomic resolution under negative charging. The gel clusters of sulfobetaine connected with each other and gradually paved around the surface of the electrode particle.

sulfobetaine molecules' connection head to tail. The volume of acetylene black shrank as that clearly presented in Movie S2 (Supporting Information). This can be explained by the fact that the zwitterionic sulfobetaine molecules attach to the negatively charged electrode with its positive hydrophobic group and is capable of expelling water stored in the loose structure of acetylene black. The string of sulfobetaine molecules attached to the surface of electrode further grew in length by connecting additional molecules until at certain moment nano-clustering of sulfobetaine molecules occurred at the near surface with frequent reshaping (as marked by the blue arrows in Figure 2a). Later the clusters of sulfobetaine molecules wrapped around the surface of the carbon electrode, forming a waterproof layer. Therefore, as shown in the schematic in Figure 2b, our in situ HRTEM observations indicate that the formation of the waterproof layer seems to involve three stages of structural evolution: the initial directional adsorption of sulfobetaine molecules to

the electrode surface, the lengthening of the molecules' string, and the clustering of the sulfobetaine molecules. The morphology of the waterproof layer depends on the surface roughness of the electrode. Protrusions would appear at the salient points on the electrode. However, if the electrode surface is relatively flat, the waterproof layer can be quite uniform in thickness. Figure 2c and Movie S3 (Supporting Information) show the dynamic process of the formation of the waterproof layer at atomic resolution on an individual acetylene black particle in spherical shape with diameter at ≈ 30 nm. It was observed that except one protrusion, the waterproof layer gradually formed at different places and further connected with each other and paved around the surface of the electrode particle. The thickness of the waterproof layer was only ≈ 5 nm. The shrink rate of the carbon electrode's diameter is calculated as 0.0315 nm s^{-1} (Figure S3, Supporting Information). During the entire process, the atomic structure of the acetylene black near the

surface maintained the same and no gas bubble was observed, indicating that no chemical reaction occurred during the successful impediment of water electrolysis.

The distribution of zwitterionic additives and charged ions on the electrode surface at different working voltages were systematically studied by using high-resolution scanning transmission electron microscope (HRSTEM) and energy-dispersive X-ray spectroscopy (EDS) to provide chemical information that complemented the in situ observations on structural evolution. The cross-section TEM samples of the electrode in the bulk counterparts were lift-out from the surface of 0.5 V charged, 1.0 V charged and discharged negative electrode materials in NaNO₃-Sulfobetaine/H₂O electrolytes, respectively. The signal of C, Na, and S represents the information of electrode, positive ion in electrolyte and sulfobetaine additive, respectively. The signal of O can come from sulfobetaine additive and NO₃⁻. However, considering the negligible X-ray signal of N, the majority of the O signal should come from the sulfobetaine additive. **Figure 3a** shows a series of high-angle annular dark field (HAADF) images of the porous carbon electrode together with the EDS mapping. As seen in **Figure 3a**, as the electrode was polarized to -0.5 V, S shows slight accumulation along the surface of mesopores of the carbon electrode. The accumulation of O in the same configuration was much more significant since the atomic ratio of O:S is 3:1 in sulfobetaine additive. It indicates that sulfobetaine molecules are preferentially adsorbed on the electrode surface, resulting in the formation of a thin waterproof layer at the electrode surface. As the potential reached -1 V, the signals of Na, O, and S elements were remarkably increased around the surface of mesopores of carbon electrode. Significant aggregation of S and O was observed within the mesopores, indicating the growth of the waterproof layer due to the further clustering of sulfobetaine molecules. Meanwhile, the electrostatic interaction with charged electrode became stronger so that Na⁺ ions passed through the waterproof layer and were electroadsorbed at the electrode surface eventually. After reducing the potential from -1 V back to 0 V, the adsorbed sulfobetaine and Na⁺ ions were obviously eliminated at the electrode surface after discharging. These results were quite consistent with the in situ observations as well.

Accompanied with the formation of the waterproof layer at the electrode surface, the structure of the solutions also changed obviously in the bulk phase of the liquid cell upon charging. **Figure 3b** displays the time-series snapshots of the solutions captured from **Movie S4** (Supporting Information). Initially, the NaNO₃-Sulfobetaine/H₂O solution showed a relatively uniform liquid film. Upon charging, the sulfobetaine molecules underwent self-assembly in the bulk liquid phase. The bright field TEM contrast indicates that during this process, the sulfobetaine molecules formed nanosized clusters with circular shape. This process indicates that the sulfobetaine preferentially self-assembly aggregates by connecting its negatively charged hydrophilic group to the positively charged hydrophobic group of another molecule under electric field, which is able to leave high freedom for water molecules to conduct ions in the bulk solutions.

With such an anti-electrolytic zwitterionic waterproofing strategy, the electrochemical stability window of the aqueous

electrolyte could be significantly enhanced without sacrificing ionic conductivity. To test this concept, betaine is introduced into traditional NaNO₃ solution to prepare 2 M NaNO₃-*x*Betaine/H₂O electrolytes, where *x* represents the weight ratio of betaine and H₂O (Experimental Section). It was found that the overall electrochemical stability window of betaine-based NaNO₃ electrolyte was largely expanded, while its ionic conductivity was superior to the traditional nonionic-additive counterparts. As shown in **Figure 4a**, 2 M NaNO₃-0.9Betaine/H₂O electrolyte showed a wide electrochemical stability window of 2.73 V, which was measured by linear sweep voltammetry tests at 20 mV s⁻¹ versus Ag/AgCl. Especially, the cathodic limit potential was effectively decreased from -0.43 V in 2 M NaNO₃ solution to -1.43 V in 2 M NaNO₃-0.9Betaine/H₂O electrolytes, pushing the hydrogen reaction potential well beyond the electrochemical stability window of bulk water. Meanwhile, as shown in **Figure 4b**, the ionic conductivity is up to 26 mS cm⁻¹, much higher than those of conventional nonionic additive approaches (0.8–3.376 mS cm⁻¹). In addition, one can even expand the cathodic limit potential to -1.53 V and the overall electrochemical stability window to 2.83 V (**Figure S4**, Supporting Information) by further increasing the concentration of betaine (2 M NaNO₃-1.3Betaine/H₂O). The same electrochemical testing was performed on NaNO₃-Sulfobetaine/H₂O electrolyte as well. The overall electrochemical stability window was expanded to 2.76 V (**Figure S5**, Supporting Information) with the ionic conductivity remaining high (10.42 mS cm⁻¹). Besides, two additional zwitterionic additives 3-[Decyl(dimethyl)ammonio]-1-propanesulfonate (C₁₅H₃₃NO₃S) and 3-[Dodecyl(dimethyl)ammonio]-1-propanesulfonate (C₁₇H₃₇NO₃S) are tested as well, the detailed methods are presented in Experimental Section. The electrochemical stability windows and ionic conductivities of the two electrolytes with zwitterionic additives are measured as 2.71 V/40.1 mS cm⁻¹ and 2.67 V/45 mS cm⁻¹, respectively (**Figures S6** and **S7**, Supporting Information).

Benefiting from the above merits, the zwitterion-based electrolyte enables the construction of high-performance supercapacitors. The electrochemical performances using betaine-based and nonionic additive-based electrolytes (2 M NaNO₃-0.9Betaine/H₂O and 2 M NaNO₃/66.7 wt.% sucrose) are comprehensively compared. Symmetric supercapacitor coin cells using commercial activated carbon YP-50F electrodes are assembled, and the detailed fabrication process can be found in Experimental Section. Importantly, due to the moisture-tolerant and environmentally friendly properties of the electrolytes, the assembly process of supercapacitor cells can be conveniently performed in the ambient atmosphere without a glove box. The supercapacitors using 2 M NaNO₃-0.9Betaine/H₂O electrolyte displayed significant optimization in terms of both capacitance and resistance. The cyclic voltammogram (CV) curve of 2 M NaNO₃-0.9Betaine/H₂O electrolyte at a scan rate of 200 mV s⁻¹ shows an approximately rectangular shape, indicating a good capacitive behavior (**Figure 4c**). The CV curves at other scan rates can be found in **Figures S8** and **S9** (Supporting Information). Smaller IR drop of the galvanostatic charge/discharge (GCD) curves of 2 M NaNO₃-0.9Betaine/H₂O electrolyte is observed (**Figure 4d**). According to the electrochemical impedance spectroscopy (**Figure 4e**) and equivalent circuit fitting results (**Figure S10**, Supporting Information), the charge

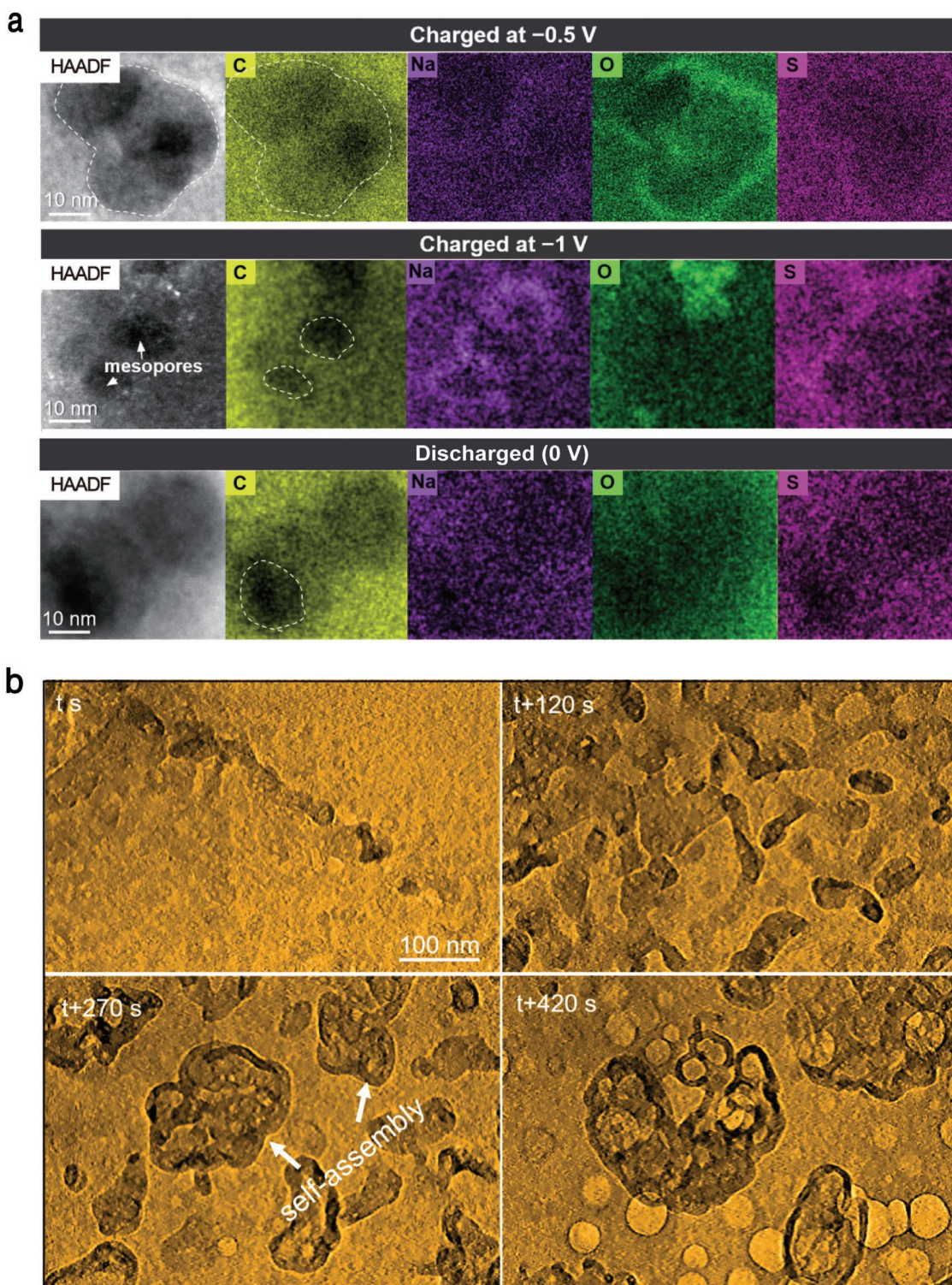


Figure 3. HAADF-STEM images and EDS mapping of the porous carbon electrodes with different charging conditions, and the HRTEM images showing the self-aggregation of sulfobetaine in the bulk liquid phase. a) HAADF-STEM images of carbon electrode at varying voltages and the corresponding EDS maps for typical elements involved of C, Na, O, and S. Significant accumulation of additives, and Na⁺ can be observed at the electrode surface when the electrode is polarized to near maximum potential. b) The time-series TEM images of the bulk liquid phase of the NaNO₃-Sulfobetaine/H₂O solutions under electric field. The sulfobetaine molecules were separated from the solution and formed the nanosized clusters with hydrophilic sulfur-containing groups on the periphery and other hydrophobic groups on the inner layer.

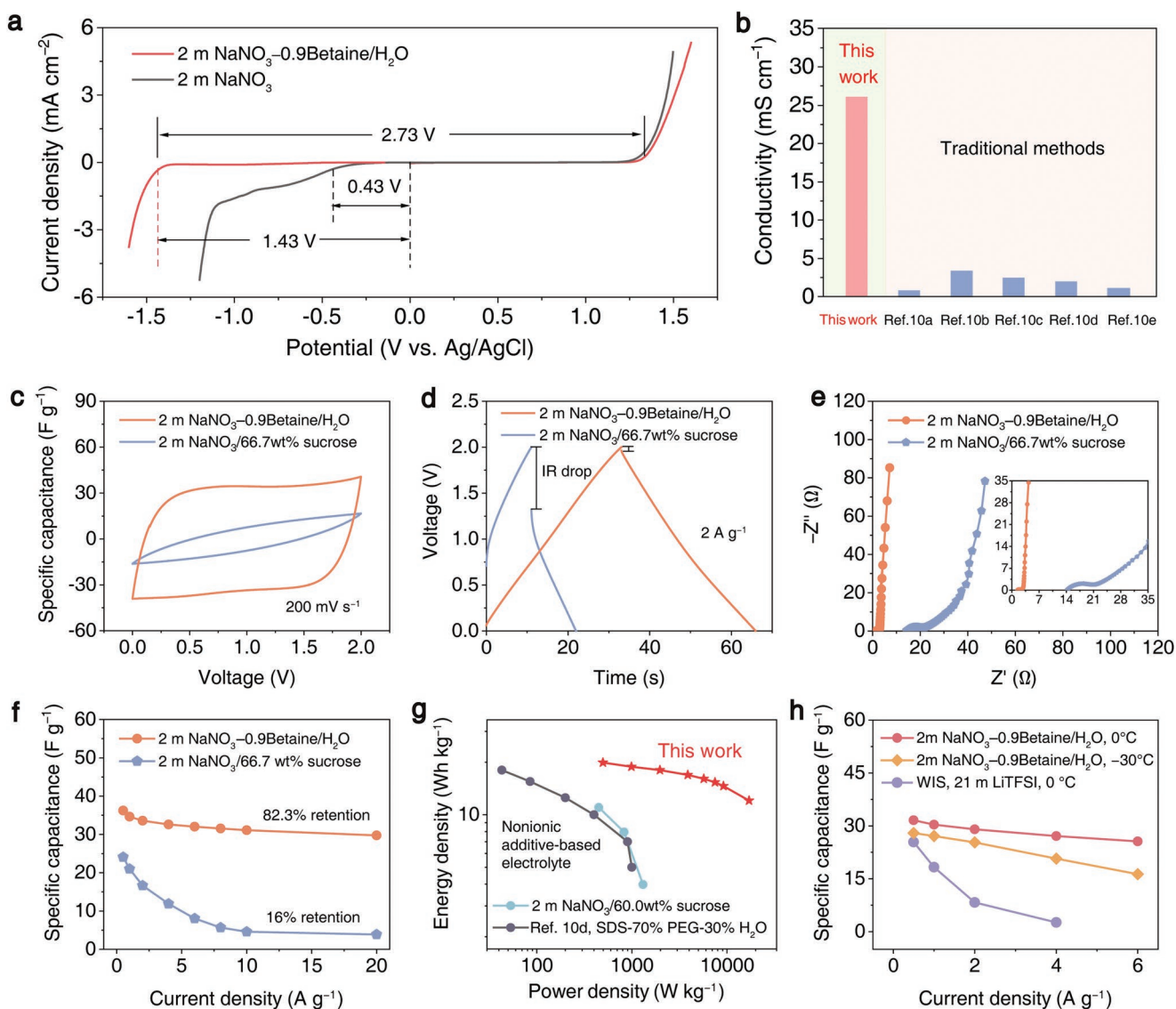


Figure 4. Electrochemical performance of the carbon-based supercapacitors. a) Comparison of the electrochemical stability windows for 2 M NaNO₃ and 2 M NaNO₃-0.9Betaine/H₂O electrolytes determined by linear sweep voltammetry versus Ag/AgCl. b) Comparison of ionic conductivities between zwitterionic additive-based electrolyte and conventional nonionic additive-based electrolytes when similar electrochemical stability windows are achieved. c,d,e,f) Comparison of CV curves (200 mV s⁻¹) (c), GCD curves (2 A g⁻¹) (d), Nyquist plots (e) and rate performance (f) of the supercapacitors using the 2 M NaNO₃-0.9Betaine/H₂O electrolyte and 2 M NaNO₃/66.7 wt.% sucrose. g) Ragone plots of the power and energy densities of our supercapacitors in comparison with previously reported aqueous electrolyte supercapacitors. h) Comparison of the specific capacitance between supercapacitors using 2 M NaNO₃-0.9Betaine/H₂O electrolytes and WIS electrolyte at different current densities and temperatures.

transfer resistance (R_{ct}) and equivalent series resistance (R_s) are 0.12 and 0.41 Ω cm² for 2 M NaNO₃-0.9Betaine/H₂O systems, respectively, which are significantly lower than those of 2 M NaNO₃/66.7 wt.% sucrose (1.64 and 4.01 Ω cm², respectively), confirming the smaller resistance for ion transportation. Consequently, upon a 40-fold current density increase from 0.5 to 20 A g⁻¹, a superior capacitance retention of 82.3% (from 36.2 to 29.8 F g⁻¹) is recognized for 2 M NaNO₃-0.9Betaine/H₂O system, in contrast to the value of 16% (from 24.22 to 3.87 F g⁻¹) in 2 M NaNO₃/66.7 wt.% sucrose (Figure 4f). Due to the large electrochemical stability window and high ionic conductivity, supercapacitors using 2 M NaNO₃-0.9Betaine/H₂O electrolyte

exhibit superior energy density and power density as evidenced by the Ragone plots in Figure 4g.

As shown in Figure S11 (Supporting Information), supercapacitors using 2 M NaNO₃-0.9Betaine/H₂O shows a high capacitance retention of 85% after 20,000 cycles at 5 A g⁻¹ with nearly 100% coulombic efficiency, demonstrating the advantages of our new method beyond the traditional SEI strategy. Meanwhile, since betaine is capable of destroying the hydrogen-bond network of water,^[14] using betaine would put down the freezing point of water to even lower. Differential scanning calorimetry (DSC) measurements show that the thermogram of the 2 M NaNO₃-1.3Betaine/H₂O electrolyte is a completely flat

line, indicating that there is no obvious phase change within a wide temperature range of 80 to -90 °C (Figures S12a and S12b, Supporting Information). Considering that the temperature limit of WIS electrolyte employing traditional SEI layer is only ≈ 10 °C,^[9d] using zwitterionic betaine additives is obviously beneficial for energy storage at low-temperature environment (Figure 4h).

3. Conclusion

The results above demonstrated that the as-proposed antielectrolytic zwitterionic waterproofing strategy is capable of suppressing interfacial electrolysis of aqueous electrolytes with negligible influence on ion transport in bulk solution. The qualified zwitterionic additives should contain the following characters: 1) owning negatively and positively charged ends with opposite wettability in monomeric unit, which can orient themselves precisely in electrostatic adsorption to form the waterproof layer that can suppress electrolysis at the solid-liquid interface and 2) their self-aggregation in electrolyte is energetically favorable and would not confine free water so that ion pairing can be avoided in bulk liquid phase. Since our strategy relies on physical electrostatic interactions not chemistry, it is applicable to not only sodium-contained electrolyte but also lithium and potassium salt electrolytes (the data was listed in Figure S13, Supporting Information) that are widely used for aqueous electrolyte energy storage devices. Such a general concept of controlling the interfacial structural evolution is scientifically important since it is free of the issues associated with chemical reactions, which is less sustainable and is generally not applicable to dilute aqueous electrolytes.^[6,7,15] Our results shed light on designing high-voltage and highly-conductive aqueous electrolytes with high adaptive capacity to environments for sustainable energy storage devices. One can expect that, a series of zwitterion-based aqueous electrolytes can be further explored based on this strategy, which may even push the performance of EES devices to new high.

4. Experimental Section

Materials and Characterizations: Electrolytes were prepared by molality (mol kg^{-1}), abbreviated as *m*. Zwitterion-based electrolytes were prepared by mixing betaine ($\text{C}_5\text{H}_{11}\text{NO}_2$) with deionized water at different weight ratios (0.9 and 1.3), abbreviated as 0.9Betaine/ H_2O and 1.3Betaine/ H_2O for simplicity. Then 2 *m* NaNO_3 were dissolved into the Betaine/ H_2O solution to formulate 2 *m* NaNO_3 -0.9Betaine/ H_2O and 2 *m* NaNO_3 -1.3Betaine/ H_2O electrolytes. And 2 *m* KNO_3 , 2 *m* LiNO_3 , and 1 *m* Li_2SO_4 were dissolved into the Betaine/ H_2O solution to formulate 2 *m* KNO_3 -0.9Betaine/ H_2O , 2 *m* LiNO_3 -0.9Betaine/ H_2O , and 1 *m* Li_2SO_4 -0.9Betaine/ H_2O , respectively. The NaNO_3 -Sulfobetaine/ H_2O electrolyte was prepared by dissolving 2 *m* NaNO_3 and sulfobetaine-8 (3-(Dimethyloctylazaniumyl)propane-1-sulfonate, $\text{C}_{13}\text{H}_{29}\text{NO}_3\text{S}$) in deionized water at a Sulfobetaine/ H_2O weight ratio of 1.4. 3-[Decyl(dimethyl)ammonio]-1-propanesulfonate ($\text{C}_{15}\text{H}_{33}\text{NO}_3\text{S}$) was added into the 2 *m* NaNO_3 aqueous electrolyte at a betaine to water weight ratio of 0.7 to construct NaNO_3 - $\text{C}_{15}\text{H}_{33}\text{NO}_3\text{S}$ / H_2O electrolyte. 3-[Dodecyl(dimethyl)ammonio]-1-propanesulfonate ($\text{C}_{17}\text{H}_{37}\text{NO}_3\text{S}$) was added into the 2 *m* NaNO_3 at a betaine to water weight ratio of 0.6 to construct NaNO_3 - $\text{C}_{17}\text{H}_{37}\text{NO}_3\text{S}$ / H_2O electrolyte. The 2 *m* NaNO_3 /66.7wt% sucrose electrolyte were fabricated by adding 2 *m* NaNO_3 in 66.7 wt.% sucrose aqueous

solution (5.84 mol kg^{-1}) according to the literature.^[10b] Lithium bis (trifluoromethane sulfonyl) imide (LiTFSI) was mixed with deionized water to create a 21 *m* LiTFSI solution. All the aqueous solutions were fabricated in the ambient atmosphere at room temperature. The ionic conductivities of electrolytes were measured by a conductivity meter (DDSJ-308F, Shanghai). The thermal properties of the electrolyte were carried out by Differential scanning calorimetry Q2000 (TA Instruments) within the -90 to 80 °C temperature range under a scan rate of 5 °C min^{-1} .

Electrochemical Measurements: The electrodes used for the assembly of supercapacitor coin cells were prepared as follows: YP-50 commercial activated carbon (AC, YP-50F, Kuraray Chemical, Japan), carbon black, styrene-butadiene rubber (SBR), and carboxymethyl cellulose (CMC) were mixed homogeneously with a ratio of 85:10:3:2. The obtained mixture was stirred in the vacuum and coated on stainless steel current collectors, and then the electrodes were dried at 60 °C for 3 h under vacuum. The mass loadings of the electrodes were $\approx 2.6 \text{ mg cm}^{-2}$. The supercapacitor coin cells were assembled by different electrolytes using two AC electrodes separated with a glass fiber membrane. Contributing to the eco-friendly and moisture-resistant property of the betaine-based electrolytes, the entire preparation and assembly process of the supercapacitors were completely carried out in the ambient atmosphere without using any moisture-free treatments. Cyclic voltammetry (CV), linear sweep voltammetry (LSV), galvanostatic charge/discharge (GCD) and electrochemical impedance spectroscopy (EIS) tests were carried out using an electrochemical workstation (PGSTAT302N, Metrohm Autolab B.V.). The electrochemical stability window of electrolytes was determined using three-electrode devices with stainless steel electrodes and Ag/AgCl (in a 3 *m* KCl aqueous solution) reference electrode. EIS measurements were executed with 5 mV amplitude over the frequency range from 0.01 Hz to 100 kHz. Low-temperature electrochemical performance tests were carried out in a temperature and humidity chamber (Dongguan Kowin Testing Equipment).

Accordingly, the specific capacitance C (F g^{-1}) of the supercapacitor was calculated based on GCD curves according to the following Equation (1):

$$C = It/V \quad (1)$$

where I (A g^{-1}) is the discharge current density, t (s) is the discharge time obtained in GCD measurements, and V (V) is the potential window after voltage drop. The mass of electrodes is calculated by their total mass.

The specific energy density E (Wh kg^{-1}) and power density P (W kg^{-1}) based on GCD curves are calculated using Equation (2) and (3).

$$E (\text{Wh kg}^{-1}) = 0.5CV^2/3.6 \quad (2)$$

$$P (\text{W kg}^{-1}) = E \times 3600/t \quad (3)$$

where t (s) is the discharge time, V (V) is the potential window after voltage drop, C (F g^{-1}) is the total capacitance of supercapacitor.

The coulombic efficiency, η , measured in GCD tests is estimated by

$$\eta = \frac{t_d}{t_c} \times 100\% \quad (4)$$

where t_d and t_c (s) represent the discharge and charge time, respectively.

DFT Calculations: The binding energy calculations between betaine (sulfobetaine), water, and ions were performed using the GAUSSIAN 09 program with the 6-311 G* basis set^[16] at the B3LYP level.^[17] The calculated values and optimized morphologies are collected in the Tables S1 and S2 (Supporting Information), where the solvation shells for Na^+ and NO_3^- ions are taken from the trajectory of the molecular dynamics simulations.

Molecular Dynamics (MD) Simulations: All MD simulations were carried out using the GROMACS 2016.2 simulation package^[18] in rectangular simulation boxes under 3D periodic boundary conditions. The GROMOS54A7 force field^[19] for betaine, water, and graphene sheets

were employed in the simulation. The force field parameters for all ions were taken from Xie et al.^[20] The simulation cell contains 189 Na⁺ ions, 189 NO₃⁻ ions, 726 betaines, and 5252 water molecules. The dimensions of the cell after equilibration are $L_x \times L_y \times L_z = 60.77 \text{ \AA} \times 60.77 \text{ \AA} \times 101.28 \text{ \AA}$, including a thickness of $\approx 25 \text{ \AA}$ vacuum in the z-axis beyond the electrolyte solutions to avoid the interactions between two graphene sheets. We imposed electric field E_z of 0.2, 0.3, 0.4, and 0.5 V nm⁻¹ along the z-axis on the electrolyte solution with a thickness of $\approx 75 \text{ \AA}$ to mimic the electrochemical condition in experiments. Energy minimization of the initial configuration was performed using a steeped descent algorithm. Then the energy minimized configuration was equilibrated in the isothermal-isobaric (NPT) ensemble for 135 ns with configurations recorded every 10 ps. Temperature was kept at the room temperature with the Nosé–Hoover thermostat^[21] using a 0.4 ps coupling time. Pressure was set at 1 bar with the Parinell–Rahman barostat^[22] using a 2 ps coupling time. All simulations used a 1.5 nm Lennard–Jones and short-range Coulombic interaction cutoff. Long-range electrostatics were computed using Particle–Mesh Ewald summation.^[23] Dynamics were propagated with a leap-frog Verlet integrator^[24] using a 2 fs time step.

In Situ Liquid Cell High-Resolution Transmission Electron Microscope (HRTEM) Measurement: Liquid cells with a 10 nm-thick low-stress SiNx observation window matching with an electrochemical TEM holder were engaged for in situ HRTEM study (CHIP-NOVA, China). Two 30 nm-thick Au electrodes with a face-to-face distance of 20 μm were deposited as the working electrode (WE) and counter electrode (CE). Before the assembly of liquid cells, acetylene black was used as the electrode material, transferred on the WE of bottom chip for real-time observation. The NaNO₃–Sulfobetaine/H₂O electrolyte was prepared by dissolving 2 m NaNO₃ and sulfobetaine-8 (3-(Dimethyl-octylazaniumyl)propane-1-sulfonate, C₁₃H₂₉NO₃S) in deionized water at a Sulfobetaine/H₂O weight ratio of 1.4, followed by stirring overnight. To avoid the evaporation of H₂O, the entire process of electrolyte injection and chip sealing was performed in the vapor-saturated glove box. The as-prepared electrolyte was added into a reservoir of liquid cell using a syringe. Then, epoxy was used to seal the reservoirs, and the liquid cell needed to stand for 12 h to stabilize the internal solution environment. An external electric field of -1 V was controlled by an electrochemical workstation (CHI 660E). In situ EC-TEM experiment was carried out in a FEI Talos (200 kV, USA).

Statistical Analysis: All the electrochemical measurements were conducted for at least three times to ensure repeatability. The figures were plotted by Origin 2018 and Adobe Illustrator CC 2018. The diameter of the carbon electrode in the TEM image was measured using ImageJ software. The fitting curves for the Nyquist spectra were analyzed by Nova 2.1 software.

Supporting Information

Supporting Information is available from the Wiley Online Library or from the author.

Acknowledgements

M.Z. and S.Z. contributed equally to this work. Z.B. was funded by the National Natural Science Foundation of China (No. 52076188 and 51621005) and Royal Society Newton Advanced Fellowship (No. 52061130218). Q.Y. was funded by National Key Research and Development Program of China (No. 2017YFA0208200) and National Natural Science Foundation of China (No. 51671168 and 51871197). K.O. acknowledges partial support from the Australian Research Council (ARC) and QUT Centre for Materials Science.

Conflict of Interest

The authors declare no conflict of interest.

Data Availability Statement

The data that support the findings of this study are available from the corresponding author upon reasonable request.

Keywords

aqueous electrolytes, electrochemical stability window, in situ transmission electron microscopy, ion conductivity, physical zwitterionic waterproofing

Received: June 22, 2022

Revised: July 25, 2022

Published online: August 31, 2022

- [1] a) K. Xu, *Nat. Energy* **2021**, *6*, 763; b) Q. Dou, L. Liu, B. Yang, J. Lang, X. Yan, *Nat. Commun.* **2017**, *8*, 2188; c) L. Smith, B. Dunn, *Science* **2015**, *350*, 918; d) M. Li, C. S. Wang, Z. W. Chen, K. Xu, J. Lu, *Chem. Rev.* **2020**, *120*, 6783.
- [2] a) D. L. Han, C. J. Cui, K. Y. Zhang, Z. X. Wang, J. C. Gao, Y. Guo, Z. C. Zhang, S. C. Wu, L. C. Yin, Z. Weng, F. Y. Kang, Q. H. Yang, *Nat. Sustain.* **2022**, *5*, 205; b) C. Zhong, B. Liu, J. Ding, X. R. Liu, Y. W. Zhong, Y. Li, C. B. Sun, X. P. Han, Y. D. Deng, N. Q. Zhao, W. B. Hu, *Nat. Energy* **2020**, *5*, 440; c) C. S. Rustomji, Y. Yang, T. K. Kim, J. Mac, Y. J. Kim, E. Caldwell, H. Chung, S. Meng, *Science* **2017**, *356*, 1351; d) V. K. Davis, C. M. Bates, K. Omichi, B. M. Savoie, N. Momcilovic, Q. Xu, W. J. Wolf, M. A. Webb, K. J. Billings, N. H. Chou, *Science* **2018**, *362*, 1144; e) C. Zhong, Y. D. Deng, W. B. Hu, J. L. Qiao, L. Zhang, J. J. Zhang, *Chem. Soc. Rev.* **2015**, *44*, 7484; f) B. Pal, S. Y. Yang, S. Ramesh, V. Thangadurai, R. Jose, *Nanoscale Adv* **2019**, *1*, 3807.
- [3] a) A. Hammami, N. Raymond, M. Armand, *Nature* **2003**, *424*, 635; b) C. P. Grey, J. M. Tarascon, *Nat. Mater.* **2017**, *16*, 45; c) W. Tang, Y. S. Zhu, Y. Y. Hou, L. L. Liu, Y. P. Wu, K. P. Loh, H. P. Zhang, K. Zhu, *Energy Environ. Sci.* **2013**, *6*, 2093; d) H. Kim, J. Hong, K. Y. Park, H. Kim, S. W. Kim, K. Kang, *Chem. Rev.* **2014**, *114*, 11788.
- [4] a) M. Chen, J. D. Wu, T. Ye, J. Y. Ye, C. Zhao, S. Bi, J. W. Yan, B. W. Mao, G. Feng, *Nat. Commun.* **2020**, *11*, 5809; b) Y. M. Sui, X. L. Ji, *Chem. Rev.* **2021**, *121*, 6654; c) N. T. Suen, S. F. Hung, Q. Quan, N. Zhang, Y. J. Xu, H. M. Chen, *Chem. Soc. Rev.* **2017**, *46*, 337; d) Z. X. Liu, Y. Huang, Y. Huang, Q. Yang, X. L. Li, Z. D. Huang, C. Y. Zhi, *Chem. Soc. Rev.* **2020**, *49*, 643; e) D. L. Chao, S. Z. Qiao, *Joule* **2020**, *4*, 1846; f) K. Xu, C. S. Wang, *Nat. Energy* **2016**, *1*, 16161.
- [5] a) Y. Gao, Z. F. Yan, J. L. Gray, X. He, D. W. Wang, T. H. Chen, Q. Q. Huang, Y. G. C. Li, H. Y. Wang, S. H. Kim, T. E. Mallouk, D. H. Wang, *Nat. Mater.* **2019**, *18*, 384; b) K. Xu, *Chem. Rev.* **2014**, *114*, 11503; c) K. Xu, *Chem. Rev.* **2004**, *104*, 4303.
- [6] a) L. Droguet, G. M. Hobold, M. F. Lagadec, R. Guo, C. Lethien, M. Hallot, O. Fontaine, J. M. Tarascon, B. M. Gallant, A. Grimaud, *ACS Energy Lett.* **2021**, *6*, 2575; b) L. Droguet, A. Grimaud, O. Fontaine, J. M. Tarascon, *Adv. Energy Mater.* **2020**, *10*, 2002440.
- [7] a) L. M. Suo, O. Borodin, T. Gao, M. Olguin, J. Ho, X. L. Fan, C. Luo, C. S. Wang, K. Xu, *Science* **2015**, *350*, 938; b) L. Suo, O. Borodin, W. Sun, X. Fan, C. Yang, F. Wang, T. Gao, Z. Ma, M. Schroeder, A. von Cresce, S. M. Russell, M. Armand, A. Angell, K. Xu, C. Wang, *Angew. Chem., Int. Ed.* **2016**, *55*, 7136; c) Y. Yamada, K. Usui, K. Sodeyama, S. Ko, Y. Tateyama, A. Yamada, *Nat. Energy* **2016**, *1*, 16129; d) L. Jiang, L. Liu, J. Yue, Q. Zhang, A. Zhou, O. Borodin, L. Suo, H. Li, L. Chen, K. Xu, Y.-S. Hu, *Adv. Mater.* **2020**, *32*, 1904427; e) L. S. Cao, D. Li, T. Pollard, T. Deng, B. Zhang, C. Y. Yang, L. Chen, J. Vatamanu, E. Y. Hu, M. J. Hourwitz, L. Ma, M. Ding, Q. Li, S. Y. Hou, K. Gaskell, J. T. Fourkas, X. Q. Yang, K. Xu, O. Borodin, C. S. Wang, *Nat. Nanotechnol.* **2021**, *16*, 902.

- [8] Y. Yamada, J. H. Wang, S. Ko, E. Watanabe, A. Yamada, *Nat. Energy* **2019**, *4*, 269.
- [9] a) T. T. Liang, R. L. Hou, Q. Y. Dou, H. Z. Zhang, X. B. Yan, *Adv. Funct. Mater.* **2021**, *31*, 2006749; b) D. Reber, R. S. Kuhnel, C. Battaglia, *ACS Mater. Lett.* **2019**, *1*, 44; c) M. Becker, R. S. Kuhnel, C. Battaglia, *Chem. Commun.* **2019**, 55, 12032; d) Q. Y. Dou, S. L. Lei, D. W. Wang, Q. N. Zhang, D. W. Xiao, H. W. Guo, A. P. Wang, H. Yang, Y. L. Li, S. Q. Shi, X. B. Yan, *Energy Environ. Sci.* **2018**, *11*, 3212.
- [10] a) J. Xie, Z. J. Liang, Y. C. Lu, *Nat. Mater.* **2020**, *19*, 1006; b) H. Bi, X. Wang, H. Liu, Y. He, W. Wang, W. Deng, X. Ma, Y. Wang, W. Rao, Y. Chai, H. Ma, R. Li, J. Chen, Y. Wang, M. Xue, *Adv. Mater.* **2020**, *32*, 2000074; c) D. J. Dong, J. Xie, Z. J. Liang, Y. C. Lu, *ACS Energy Lett.* **2022**, *7*, 123; d) M. F. Huang, S. R. Zhen, X. L. Ren, X. Ju, *J. Power Sources* **2020**, *465*, 228265; e) J. J. Xu, X. Ji, J. X. Zhang, C. Y. Yang, P. F. Wang, S. F. Liu, K. Ludwig, F. Chen, P. Kofinas, C. S. Wang, *Nat. Energy* **2022**, *7*, 186.
- [11] a) P. Simon, Y. Gogotsi, B. Dunn, *Science* **2014**, *343*, 1210; b) H. X. Ji, X. Zhao, Z. H. Qiao, J. Jung, Y. W. Zhu, Y. L. Lu, L. L. Zhang, A. H. MacDonald, R. S. Ruoff, *Nat. Commun.* **2014**, *5*, 7; c) C. Y. Liu, X. S. Wang, W. J. Deng, C. Li, J. T. Chen, M. Q. Xue, R. Li, F. Pan, *Angew. Chem., Int. Ed.* **2018**, *57*, 7046.
- [12] a) M. Di Gioacchino, F. Bruni, M. A. Ricci, *J. Mol. Liq.* **2020**, *318*, 114253; b) Q. Shao, S. Y. Jiang, *Adv. Mater.* **2015**, *27*, 15.
- [13] S. J. Pennycook, B. Rafferty, P. D. Nellist, *Microsc. Microanal.* **2000**, *6*, 343.
- [14] X. J. Sui, H. S. Guo, P. G. Chen, Y. N. Zhu, C. Y. Wen, Y. H. Gao, J. Yang, X. Y. Zhang, L. Zhang, *Adv. Funct. Mater.* **2020**, *30*, 1907986.
- [15] J. M. Yue, J. K. Zhang, Y. X. Tong, M. Chen, L. L. Liu, L. W. Jiang, T. S. Lv, Y. S. Hu, H. Li, X. J. Huang, L. Gu, G. Feng, K. Xu, L. M. Suo, L. Q. Chen, *Nat. Chem.* **2021**, *13*, 1061.
- [16] M. J. Frisch, G. W. Trucks, H. B. Schlegel, G. E. Scuseria, M. A. Robb, J. R. Cheeseman, G. Scalmani, V. Barone, G. A. Petersson, H. Nakatsuji, X. Li, M. Caricato, A. Marenich, J. Bloino, B. G. Janesko, R. Gomperts, B. Mennucci, H. P. Hratchian, J. V. Ortiz, A. F. Izmaylov, J. L. Sonnenberg, D. Williams-Young, F. Ding, F. Lipparini, F. Egidi, J. Goings, B. Peng, A. Petrone, T. Henderson, D. Ranasinghe, et al., Gaussian 09, Revision A.02. **2009**.
- [17] P. J. Stephens, F. J. Devlin, C. F. Chabalowski, M. J. Frisch, *J. Phys. Chem.* **1994**, *98*, 11623.
- [18] D. Spoel, E. Lindahl, B. Hess, G. Groenhof, H. Berendsen, *J. Comput. Chem.* **2005**, *26*, 1701.
- [19] N. Schmid, A. P. Eichenberger, A. Choutko, S. Riniker, M. Winger, A. Mark, W. Gunsteren, *Eur. Biophys. J.* **2011**, *40*, 843.
- [20] W. J. Xie, Z. Zhang, Y. Q. Gao, *J. Phys. Chem. B* **2016**, *120*, 2343.
- [21] W. G. Hoover, *Phys. Rev. A Gen. Phys.* **1985**, *31*, 1695.
- [22] M. Parrinello, A. Rahman, *Phys. Rev. Lett.* **1980**, *45*, 1196.
- [23] T. Darden, D. York, L. Pedersen, *J. Chem. Phys.* **1993**, *98*, 10089.
- [24] W. F. Van Gunsteren, H. J. C. Berendsen, *Mol. Simul.* **1988**, *1*, 173.

Supporting Information

for *Adv. Funct. Mater.*, DOI: 10.1002/adfm.202207140

Controlling Interfacial Structural Evolution in Aqueous Electrolyte via Anti-Electrolytic Zwitterionic Waterproofing

Zheng Bo, Meiqi Zhou, Shiyuan Zhou, Yajing Song, Zhu Liu, Honggang Liao,* Huachao Yang, Jianhua Yan, Kefa Cen, Xiulin Fan, Qian Yu, Kostya (Ken) Ostrikov, and Ju Li*

1
2
3
4
5
6
7
8
9
10
11
12
13
14
15
16
17
18
19
20
21
22
23
24
25
26
27
28
29
30
31
32
33
34

Supporting Information

Controlling Interfacial Structural Evolution in Aqueous Electrolyte via Antielectrolytic Zwitterionic Waterproofing

*Zheng Bo**, *Meiqi Zhou*, *Shiyuan Zhou*, *Yajing Song*, *Zhu Liu*, *Honggang Liao**, *Huachao Yang*, *Jianhua Yan*, *Kefa Cen*, *Xiulin Fan*, *Qian Yu*, *Kostya (Ken) Ostrikov*, and *Ju Li*

Z. Bo, M. Zhou, H. Yang, J. Yan, K. Cen

State Key Laboratory of Clean Energy Utilization

College of Energy Engineering

Zhejiang University

Hangzhou 310027, China

E-mail: bozh@zju.edu.cn

S. Zhou, H. Liao

State Key Laboratory of Physical Chemistry of Solid Surfaces

Collaborative Innovation Center of Chemistry for Energy Materials

Xiamen University

Xiamen 361005, China

E-mail: hgliao@xmu.edu.cn

Y. Song, X. Fan, Q. Yu

Center of Electron Microscopy and State Key Laboratory of Silicon Materials

School of Materials Science and Engineering

Zhejiang University

Hangzhou 310027, China

Z. Liu

ZJU-Hangzhou Global Scientific and Technological Innovation Center

Hangzhou 311200, China

K. Ostrikov

35 School of Chemistry and Physics & Centre for Materials Science

36 Queensland University of Technology

37 Brisbane, Queensland, 4000, Australia

38

39 J. Li

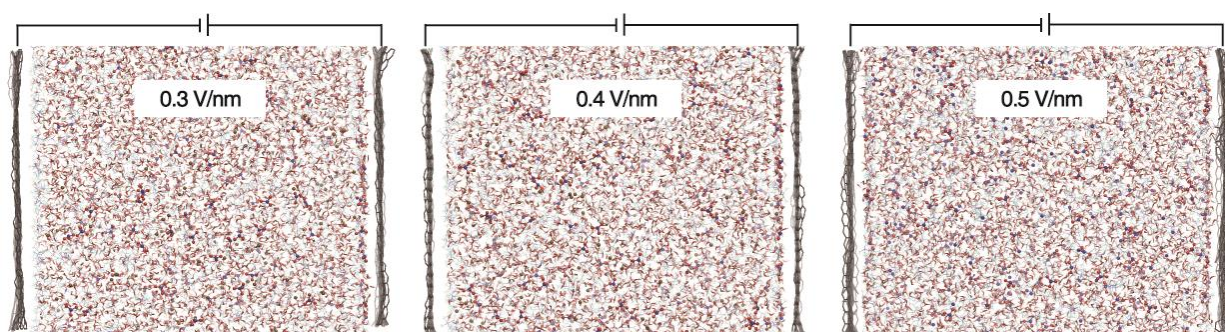
40 Department of Nuclear Science and Engineering and Department of Materials Science and

41 Engineering

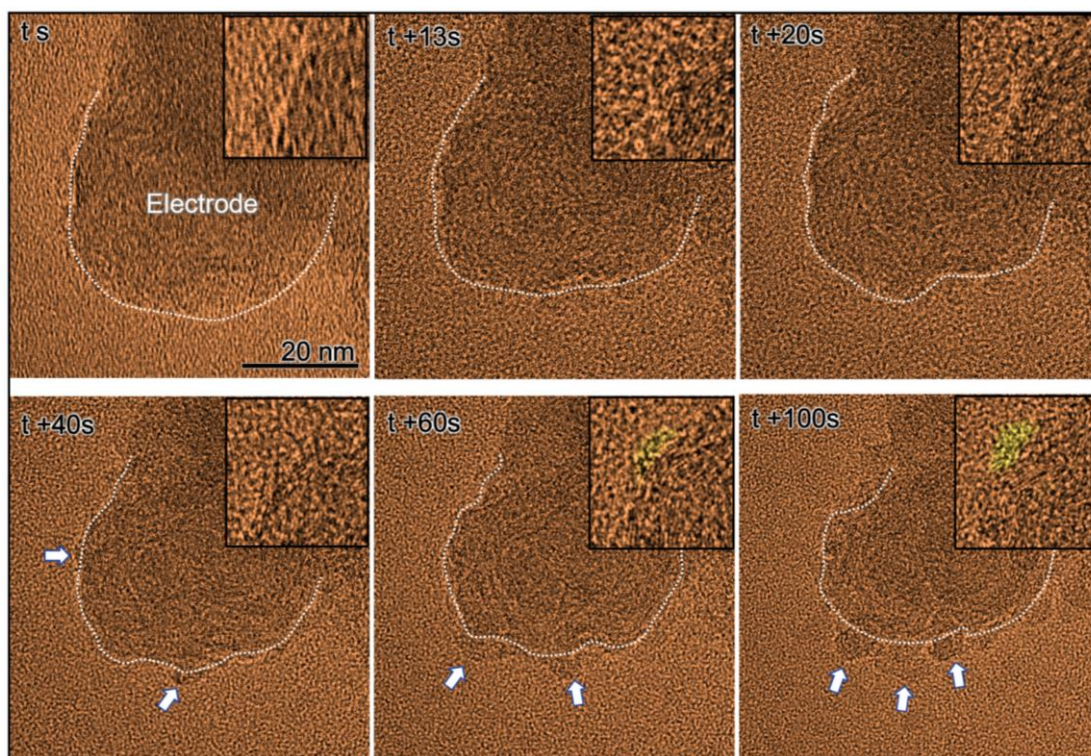
42 Massachusetts Institute of Technology

43 Cambridge, MA, 02139, USA

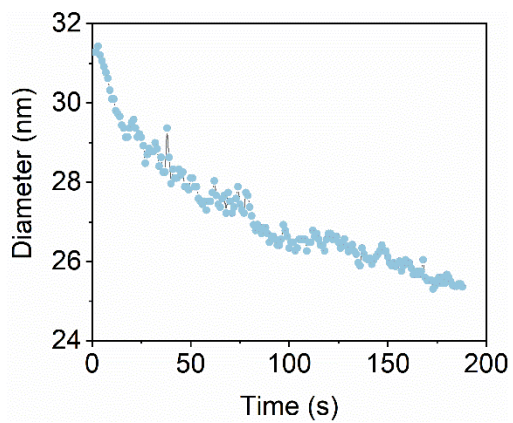
44



45
46 **Figure S1.** Snapshots showing the MD simulation pictures of the 2 m NaNO₃-
47 0.9Betaine/H₂O electrolyte under external electric field E_z of 0.3, 0.4 and 0.5 V/nm.
48

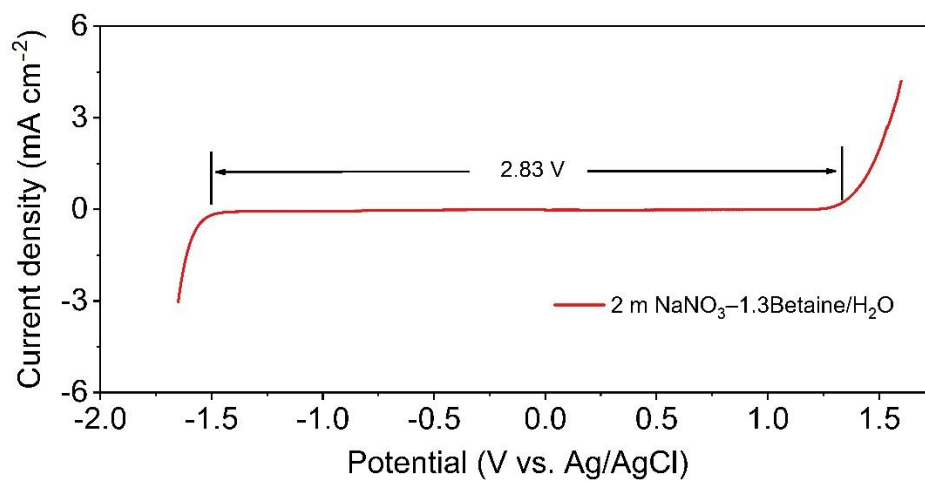


49
50 **Figure S2.** A series of HRTEM images showing the change of morphology of the electrode in
51 NaNO_3 -Sulfofetaine/ H_2O electrolyte during the negative polarization process. Significant
52 shrinkage of the electrode material was observed under electric field.
53



54
55
56

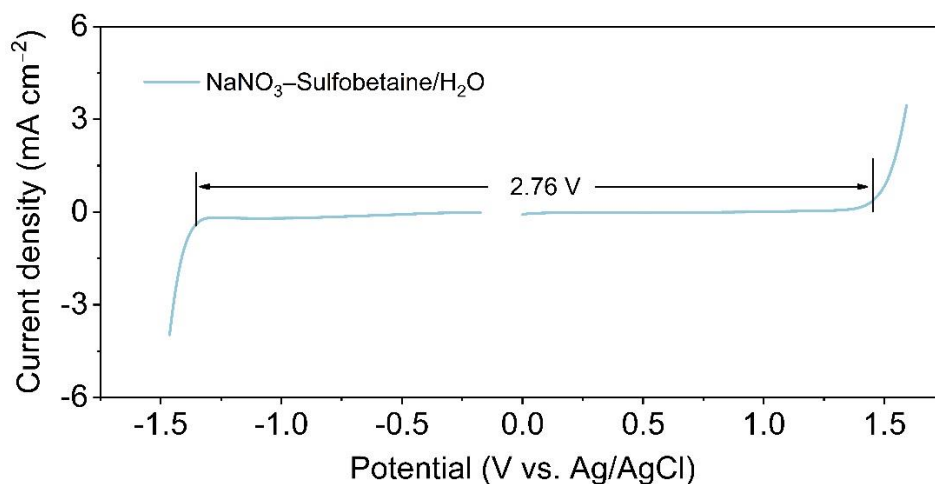
Figure S3. The shrink rate of diameter of the carbon electrode during the charging process.



57

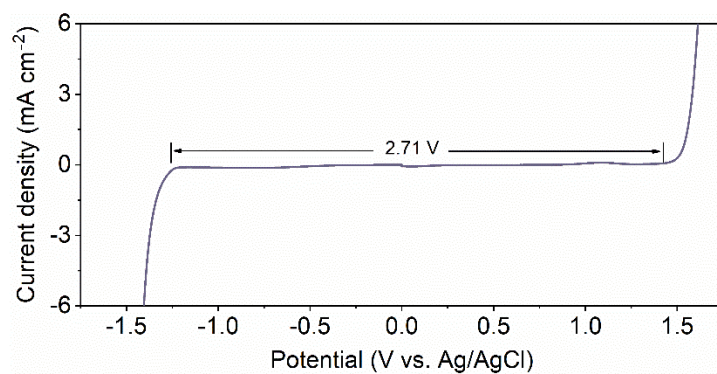
58 **Figure S4.** Electrochemical stability window for 2 m NaNO_3 -1.3Betaine/ H_2O electrolyte
59 measured by linear sweep voltammetry at a scan rate of 20 mV s^{-1} versus Ag/AgCl.

60

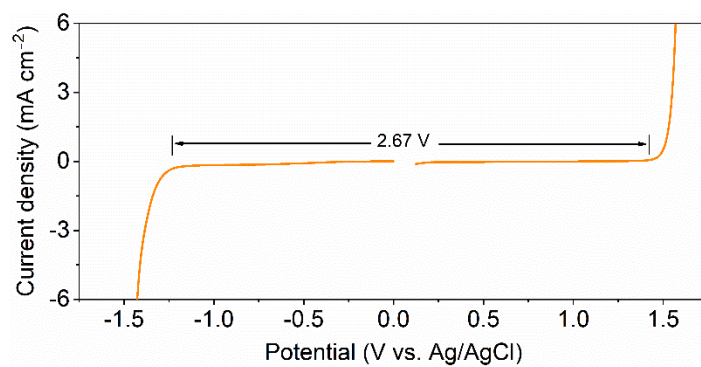


61
62 **Figure S5.** Electrochemical stability window for NaNO₃-Sulfobetaine/H₂O electrolyte
63 measured by linear sweep voltammetry at a scan rate of 20 mV s⁻¹ versus Ag/AgCl.

64 The weight ratio of the hydrophobic group to the total mass was calculated accordingly. For
65 betaine molecule, the weight ratio of the hydrophobic group to the total mass is ~0.5. So as
66 the weight ratio of betaine to water is 0.9, the weight ratio of the hydrophobic group to water
67 is ~0.4. As for sulfobetaine, due to the long chain structure, the weight ratio of its positively
68 charged hydrophobic groups to the total mass is only ~0.21. Therefore, to make the weight
69 ratio of its positively charged hydrophobic groups to water to ~0.4, the weight ratio of
70 sulfobetaine to water needs to be ~1.4.



71
72 **Figure S6.** Electrochemical stability window for $\text{NaNO}_3\text{-C}_{15}\text{H}_{33}\text{NO}_3\text{S}/\text{H}_2\text{O}$ electrolyte
73 measured by linear sweep voltammetry at a scan rate of 20 mV s^{-1} versus Ag/AgCl.
74

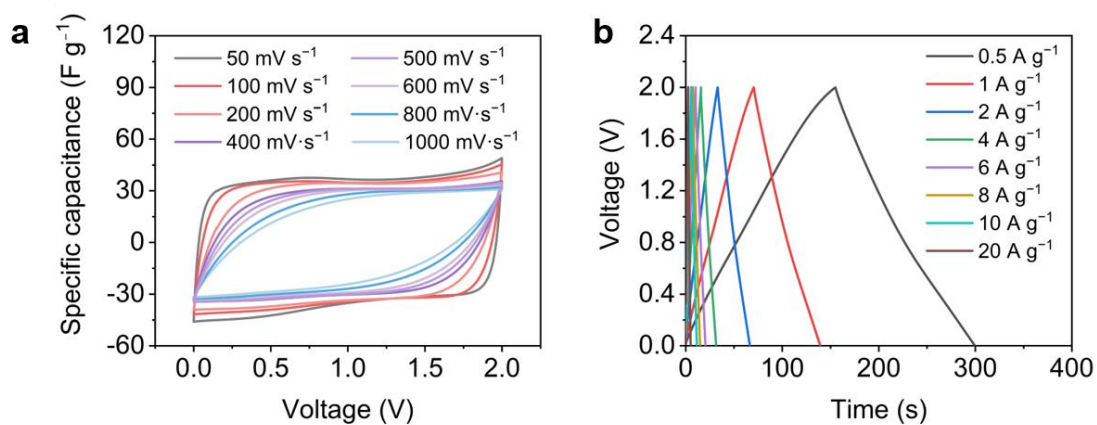


75

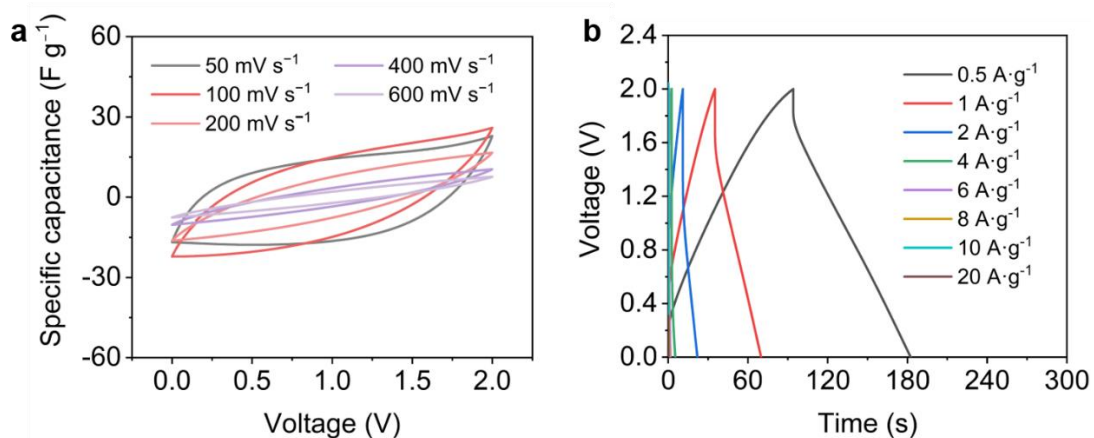
76 **Figure S7.** Electrochemical stability window for NaNO₃-C₁₇H₃₇NO₃S/H₂O electrolyte77 measured by linear sweep voltammetry at a scan rate of 20 mV s⁻¹ versus Ag/AgCl.

78

79



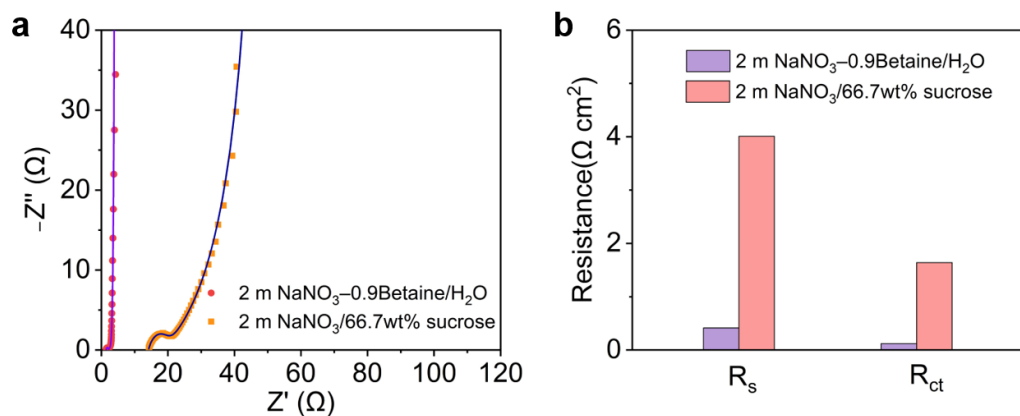
80
81 **Figure S8.** Electrochemical performance of the 2 m NaNO₃-0.9Betaine/H₂O electrolyte. (a)
82 CV curves at different scan rates and (b) GCD curves at different current densities of the
83 supercapacitor using 2 m NaNO₃-0.9Betaine/H₂O electrolyte.
84



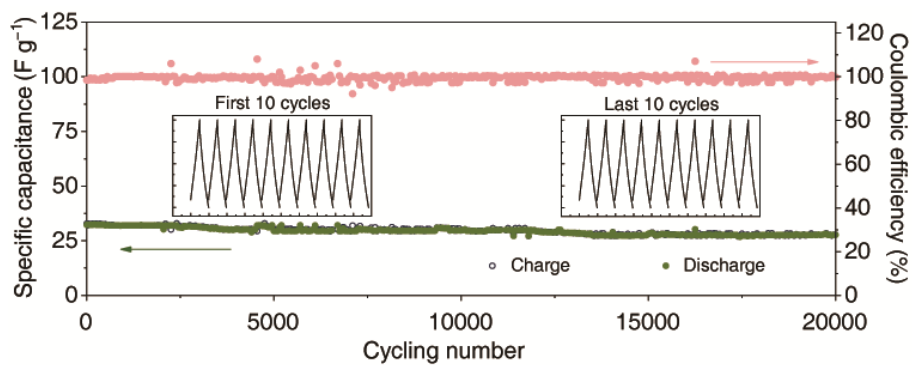
85
86 **Figure S9.** Electrochemical performance of the 2 m NaNO₃/66.7wt% sucrose electrolyte. (a)
87 CV curves at different scan rates and (b) GCD curves at different current densities of the
88 supercapacitor using 2 m NaNO₃/66.7wt% sucrose electrolyte.

89

90



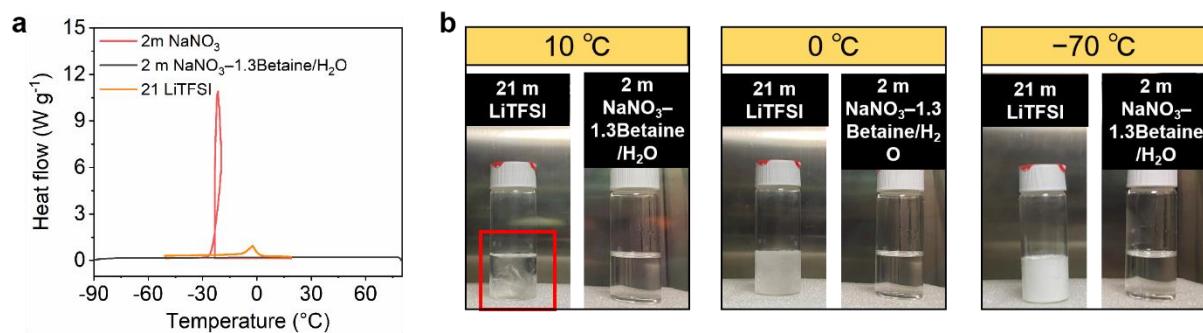
91
92 **Figure S10.** Comparison of the supercapacitors' resistance with 2 m NaNO₃-0.9Betaine/H₂O
93 electrolyte and 2 m NaNO₃/66.7wt% sucrose. (a) The fitting curves for the Nyquist spectra of
94 supercapacitors using 2 m NaNO₃-0.9Betaine/H₂O electrolyte and 2 m NaNO₃/66.7wt%
95 sucrose electrolyte. (b) The calculated equivalent series resistance (R_s) and charge transfer
96 resistance (R_{ct}) for the Nyquist spectra.
97



98

99 **Figure S11.** Cycling performance of the supercapacitor using 2 m NaNO₃-0.9Betaine/H₂O
100 electrolyte at 5 A g⁻¹

101

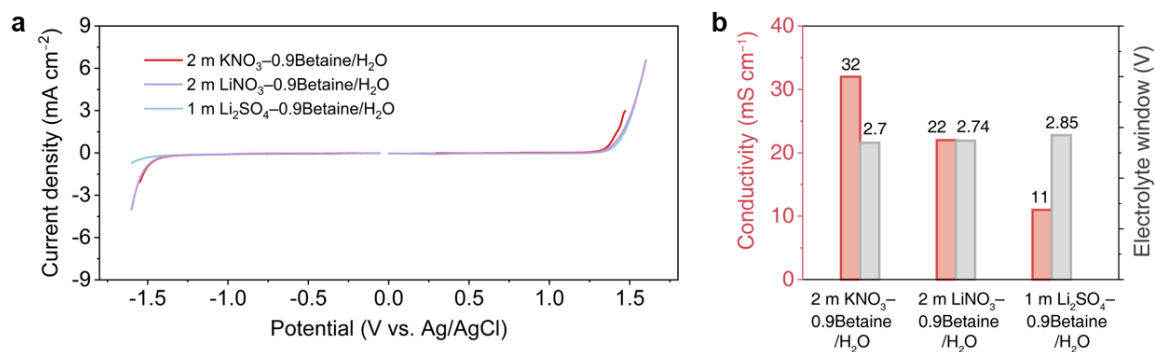


102

103 **Figure S12.** Temperature properties of the zwitterion-based electrolyte and WIS (21 m
104 LiTFSI) electrolyte. (a) Differential scanning calorimetry curves of the 2 m NaNO₃, 2 m
105 NaNO₃-1.3Betaine/H₂O and 21 m LiTFSI electrolyte. (b) Photographs showing the state of
106 21 m LiTFSI and 2 m NaNO₃-1.3Betaine/H₂O electrolyte at different temperatures. Note that
107 the salts in 21 m LiTFSI solutions precipitates at 10 °C, while the 2 m NaNO₃-
108 1.3Betaine/H₂O electrolyte is still in liquid phase at -70 °C.

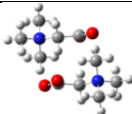
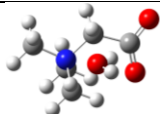
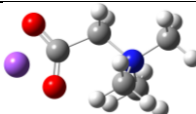
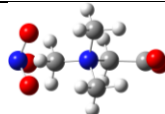
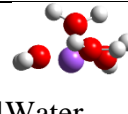
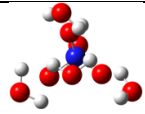
109

110



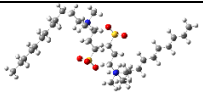
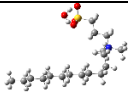
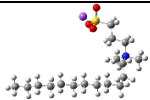
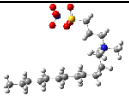

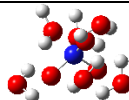
111
112 **Figure S13.** The universality and feasibility of zwitterion strategy in various aqueous
113 electrolyte. (a) Electrochemical stability windows for different electrolyte measured by linear
114 sweep voltammetry at a scan rate of 20 mV s⁻¹ versus Ag/AgCl. (b) Electrochemical stability
115 windows and ionic conductivities of different lithium and potassium salt electrolytes with
116 betaine additive.
117

118 **Table S1.** Calculated binding energy values between betaine, water, Na^+ , and NO_3^- using
 119 density functional theory (DFT) calculations. The coordination numbers of water molecules
 120 with Na^+ and NO_3^- are calculated from the molecular dynamics simulations.

						
Betaine	Betaine- Betaine	Betaine -Water	Betaine - Na^+	Betaine - NO_3^-	4Water - Na^+	5Water - NO_3^-
Binding energy (eV)	-1.42458	-0.99380	-3.11662	-1.50667	-4.98867	-2.905483

121

122 **Table S2.** Calculated binding energy values between sulfobetaine, water, Na^+ , and NO_3^- using
 123 density functional theory (DFT) calculations. The coordination numbers of water molecules
 124 with Na^+ and NO_3^- are calculated from the molecular dynamics simulations.

						
Sulfo	Sulfobetaine-	Sulfobetaine	Sulfobetaine	Sulfobetaine	5Water	6Water
-betaine	Sulfobetaine	-Water	- Na^+	- NO_3^-	- Na^+	- NO_3^-
Binding						
energy	-1.31388	-0.66514	-7.59075	-1.70944	-6.12433	-3.87318
(eV)						

125

126 **Movie S1.** The in situ HRTEM movie showing the change of morphology of the electrode in
127 NaNO₃-Sulfobetaine/H₂O electrolyte during the negative polarization process. (scale bar: 20
128 nm)

129
130 **Movie S2.** The in situ HRTEM movie demonstrating the detailed structural evolution at the
131 electrode's surface upon charging. The dynamic behaviors of individual sulfobetaine
132 molecules during charging were shown. (scale bar: 10 nm)

133
134 **Movie S3.** The in situ HRTEM movie showing the formation process of the waterproof layer
135 on the surface a single acetylene black particle.

136
137 **Movie S4.** The in situ TEM movie showing the self-aggregation of sulfobetaine molecules in
138 the bulk phase of the liquid cell upon charging. (scale bar: 100 nm)